

University of South Carolina Scholar Commons

Faculty Publications

Mechanical Engineering, Department of

2014

Influence of Crystal Structure on the Electrochemical Performance of A-Site-Deficient $\text{Sr}_{1-s}\text{Nb}_{0.1}\text{Co}_{0.9}\text{O}_{3-\delta}$ Perovskite Cathodes

Yinlong Zhu

Ye Lin

University of South Carolina - Columbia, linye@mailbox.sc.edu

Xuan Shen

Jaka Sunarso

Wei Zhou

See next page for additional authors

Follow this and additional works at: https://scholarcommons.sc.edu/emec_facpub

 Part of the [Applied Mechanics Commons](#), [Electro-Mechanical Systems Commons](#), and the [Energy Systems Commons](#)

Publication Info

Published in *RSC Advances*, Volume 48, Issue 77, 2014, pages 40865-40872.

©RSC Advances 2014, Royal Society of Chemistry.

This article cannot be redistributed or further made available. This article was first published by the Royal Society of Chemistry and can be found at <http://dx.doi.org/10.1039/c4ra06191h>

Zhu, Y., Lin, Y., Shen, X., Sunarso, J., Zhou, W., Jiang, S., Su, Dong, Chen, F., & Shao, Z. (2014). Influence of Crystal Structure on the Electrochemical Performance of A-Site-Deficient $\text{Sr}_{1-s}\text{Nb}_{0.1}\text{Co}_{0.9}\text{O}_{3-\delta}$ Perovskite Cathodes. *RSC Advances*, 4 (77), 40865 – 40872.

<http://dx.doi.org/10.1039/C4RA06191H>

This Article is brought to you by the Mechanical Engineering, Department of at Scholar Commons. It has been accepted for inclusion in Faculty Publications by an authorized administrator of Scholar Commons. For more information, please contact dillarda@mailbox.sc.edu.

Author(s)

Yinlong Zhu, Ye Lin, Xuan Shen, Jaka Sunarso, Wei Zhou, Shanshan Jiang, Dong Su, Fanglin Chen, and Zongping Shao

PAPER

 View Article Online
 View Journal | View Issue

 CrossMark
 click for updates
Cite this: *RSC Adv.*, 2014, 4, 40865

Influence of crystal structure on the electrochemical performance of A-site-deficient $\text{Sr}_{1-s}\text{Nb}_{0.1}\text{Co}_{0.9}\text{O}_{3-\delta}$ perovskite cathodes†

 Yinlong Zhu,^a Ye Lin,^b Xuan Shen,^{cd} Jaka Sunarso,^e Wei Zhou,^{*f} Shanshan Jiang,^a Dong Su,^c Fanglin Chen^b and Zongping Shao^{*g}

The creation of A-site cation defects within a perovskite oxide can substantially alter the structure and properties of its stoichiometric analogue. In this work, we demonstrate that by vacating 2 and 5% of A-site cations from $\text{SrNb}_{0.1}\text{Co}_{0.9}\text{O}_{3-\delta}$ (SNC1.00) perovskites ($\text{Sr}_{1-s}\text{Nb}_{0.1}\text{Co}_{0.9}\text{O}_{3-\delta}$, $s = 0.02$ and 0.05 ; denoted as SNC0.98 and SNC0.95, respectively), a Jahn–Teller (JT) distortion with varying extents takes place, leading to the formation of a modified crystal lattice within a the perovskite framework. Electrical conductivity, electrochemical performance, chemical compatibility and microstructure of $\text{Sr}_{1-s}\text{Nb}_{0.1}\text{Co}_{0.9}\text{O}_{3-\delta}$ as cathodes for solid oxide fuel cells were evaluated. Among SNC1.00, SNC0.98 and SNC0.95, SNC0.95 ($P4/mmm$ symmetry (#123)) which exhibits a large JT distortion in conjunction with charge-ordering of cobalt (Co) shows the best oxygen reduction reaction (ORR) activity at low temperature while SNC0.98 ($P4mm$ symmetry (#99)), which displays a local JT distortion, shows the poorest performance.

 Received 24th June 2014
 Accepted 21st August 2014

DOI: 10.1039/c4ra06191h

www.rsc.org/advances

1. Introduction

The solid oxide fuel cell (SOFC) is one of the key technologies enabling clean energy delivery with high conversion efficiency, particularly for power generation from hydrogen, carbon monoxide, methane, coal syngas, and liquid hydrocarbon fuels. The conventional SOFC nonetheless has shortcomings in terms of its high cost and degradation in performance from high temperature operation. To lower the operating temperature, the oxygen reduction reaction (ORR) activity of the SOFC cathode must be improved to maintain high power density.

ABO₃ perovskite-type mixed oxide-ionic and electronic conductors (MIECs) are among excellent cathode candidates for low-temperature SOFCs.^{1–8} Up to a reasonable limit, these perovskite oxides can fine-tune their structure (so that their original framework is maintained) to accommodate a mismatch of the equilibrium bond lengths between (and within) the A and B sites, cation and/or anion vacancies, as well as the formation of A- or B-site cation ordering structures.⁹ In this context, one strategy has been devised to enhance their oxygen reduction kinetics, *e.g.* by introducing A-site defects. Several A-site deficient perovskites, namely $\text{La}_{0.6}\text{Sr}_{0.4-s}\text{Co}_{0.2}\text{Fe}_{0.8}\text{O}_{3-\delta}$,¹⁰ $(\text{Pr}_{0.6}\text{Sr}_{0.4})_{1-s}\text{Co}_{0.2}\text{Fe}_{0.8}\text{O}_{3-\delta}$,¹¹ $\text{La}_{1-s}\text{Fe}_{0.4}\text{Ni}_{0.6}\text{O}_{3-\delta}$,^{12,13} $(\text{Ba}_{0.5}\text{Sr}_{0.5})_{1-x}\text{Co}_{0.8}\text{Fe}_{0.2}\text{O}_{3-\delta}$,¹⁴ $\text{Ba}_{1-x}\text{Co}_{0.9-y}\text{Fe}_y\text{Nb}_{0.1}\text{O}_{3-\delta}$,^{15,16} and $\text{PrBa}_{1-s}\text{Co}_2\text{O}_{5+\delta}$ (ref. 17) have been investigated as cathode materials for SOFCs. The physical and chemical properties of A-site deficient perovskites are often substantially different from those of the stoichiometric ones. The introduction of A-site defects tends to create additional oxygen vacancies which facilitate oxygen ionic transport and enhance the ORR activity.¹⁸ However, these oxygen vacancies may also interfere with the electron transport, reducing the electronic conductivity of the materials.¹⁹ We found a novel A-site deficient perovskite, $\text{Sr}_{0.95}\text{Nb}_{0.1}\text{Co}_{0.9}\text{O}_{3-\delta}$ (SNC0.95) which exhibits substantially improved ORR activity at low temperatures relative to its stoichiometric analogue, $\text{SrNb}_{0.1}\text{Co}_{0.9}\text{O}_{3-\delta}$ (SNC1.00). SNC0.95 features simultaneous enhancement in oxygen vacancy concentration and electrical conductivity,²⁰ the responsible mechanism of which has not yet been clarified. Here, we show that the $\text{Sr}_{1-s}\text{Nb}_{0.1}\text{Co}_{0.9}\text{O}_{3-\delta}$ perovskites ($s = 0.02$ and 0.05 ;

^aState Key Laboratory of Materials-Oriented Chemical Engineering, College of Chemistry & Chemical Engineering, Nanjing Tech University, No. 5 Xin Mofan Road, Nanjing 210009, P.R. China

^bDepartment of Mechanical Engineering, University of South Carolina, Columbia, South Carolina 29208, USA

^cCenter for Functional Nanomaterials, Brookhaven National Laboratory, Upton, NY 11973, USA

^dNational Laboratory of Solid State Microstructures, Department of Materials Science and Engineering, Nanjing University, Nanjing 210093, P.R. China

^eDepartment of Chemistry, University of Waterloo, 200 University Avenue West, Waterloo, Ontario, N2L 3G1, Canada

^fSchool of Chemical Engineering, The University of Queensland, Brisbane, Queensland 4072, Australia. E-mail: wei.zhou@uq.edu.au

^gState Key Laboratory of Materials-Oriented Chemical Engineering, College of Energy, Nanjing Tech University, No. 5 Xin Mofan Road, Nanjing 210009, P.R. China. E-mail: shaozp@njtech.edu.cn; Fax: +86-25-83172256

† Electronic supplementary information (ESI) available. See DOI: 10.1039/c4ra06191h

denoted as SNC0.98 and SNC0.95, respectively) exhibit different crystal structures due to the varying extent of Jahn–Teller (JT) distortions. The effects of crystal structure on the electrical conductivity, electrochemical performance, chemical compatibility and microstructure of the resultant cathode materials are examined. SNC0.95 (*P4/mmm* crystal structure) shows improved ORR activity at low temperature whereas SNC0.98 (*P4mm* structure) shows diminished performance. $\text{Sr}_{1-s}\text{Nb}_{0.1}\text{Co}_{0.9}\text{O}_{3-\delta}$ perovskites represents a deviation from the general notion of increased concentration of oxygen vacancies leading to enhanced ORR activity.^{20–22} Instead, the crystal structure seems to play a more determining role towards its electrochemical performance.

2. Experimental section

Synthesis of powders

$\text{Sr}_{1-s}\text{Nb}_{0.1}\text{Co}_{0.9}\text{O}_{3-\delta}$ ($s = 0, 0.02, 0.05, 0.1$ and 0.2) powders were synthesised using a solid-state reaction. Stoichiometric amounts of SrCO_3 , Nb_2O_5 , and Co_2O_3 (all of analytical grade, from Sinopharm Chemical Reagent Co. Ltd.) were weighed and thoroughly mixed using a planetary mill (Fritsch, Pulverisette 6) and acetone as a solvent at 400 rpm for 1 h. After drying, the powders were calcined at 1200 °C in air for 20 h. The milling and calcination were performed twice to ensure homogeneity and obtain highly pure $\text{Sr}_{1-s}\text{Nb}_{0.1}\text{Co}_{0.9}\text{O}_{3-\delta}$ phase for characterisation and testing.

Fabrication of the symmetrical cells

Symmetrical cells with an electrode| $\text{Sm}_{0.2}\text{Ce}_{0.8}\text{O}_{1.9}$ (SDC)|electrode configuration were fabricated for electrochemical impedance spectroscopy (EIS) measurements. Dense SDC disks (0.8 mm thickness, 12.5 mm diameter) were prepared by dry pressing followed by sintering at 1400 °C for 5 h. The cathode powders were firstly dispersed in a pre-mixed solution of glycerol, ethylene glycol, and isopropyl alcohol. A colloidal suspension was obtained from this mixture by a planetary milling (Fritsch, Pulverisette 6) at 400 rpm for 0.5 h. The suspension was coated by spray deposition onto both sides of the dense SDC disk and calcined at 1000 °C for 2 h in air to obtain porous electrodes. For current collection, a thin layer of silver paste was painted onto the electrode surface and dried at 100 °C.

Characterisation

The crystal structures of the powders were determined by room temperature powder X-ray diffraction (XRD, D8 Advance, Bruker, Germany) with filtered Cu-K α radiation (40 kV and 40 mA) using a receiving slit of approximately 0.2 mm. The experimental diffraction patterns were collected by scanning between $2\theta = 10$ – 90° with a step size of 0.05° . The α_2 component of the filtered radiation was stripped-off. Structure refinements of the XRD patterns were carried out using DIFFRACplus Topas 4.2 software.²³ During the refinements, general parameters such as the scale factor, background parameters, and the zero point of the counter were optimised. Le Bail

refinement was used initially to determine the space group and to approximate the lattice parameters of the SNC, SNC0.98 and SNC0.95. Rietveld refinement was then performed to determine the general position of the atoms. The oxygen occupancy is fixed to 1. It is considered futile to determine oxygen content (since oxygen has relatively low molecular weight) in the presence of heavy element using XRD pattern.

The chemical compatibility between the cathode and the SDC electrolyte materials was examined. $\text{Sr}_{1-s}\text{Nb}_{0.1}\text{Co}_{0.9}\text{O}_{3-\delta}$ –SDC powders mixtures (1 : 1 weight ratio) were calcined at 1000 °C for 2 h in air atmosphere. The phase composition of the mixture after calcinations was analysed by powder X-ray diffraction (XRD, D8 Advance, Bruker, Germany) at room temperature.

The oxygen non-stoichiometry and the valence states of cobalt at room temperature were determined by iodometric titration. In brief, approximately 0.1 g of powder was dissolved in a 6 mol L^{−1} HCl solution in a nitrogen atmosphere to prevent the oxidation of I[−] ions (from KI) by air, followed by titration with a standard thiosulfate ($\text{S}_2\text{O}_3^{2-}$) solution. The oxygen non-stoichiometry and the valence states of cobalt at high temperatures were measured by thermogravimetric analysis (TGA, Model STA 449 F3, NETZSCH) in a synthetic air atmosphere from room temperature to 1000 °C. The heating and cooling rates were 10 °C min^{−1}.

The cathode powders were packed into rectangular bars with dimensions of 2 mm × 5 mm × 20 mm and sintered at 1200 °C for 5 h in air for electrical conductivity testing. All bars used for measurements had densities of >93% of their theoretical values. Electrical conductivity was measured using a four-probe DC technique with silver coating layer as electrodes. The current and voltage were measured using a Keithley 2420 source meter; the data was collected at a 25 °C interval between 450 and 800 °C in an air atmosphere.

Raman spectra were recorded in a backscattering mode at room temperature using a LABRAM inVia micro-Raman system equipped with an optical microscope containing a 50× objective lens. The radiation source was a He–Ne laser ($\lambda = 514$ nm) operated at 1% power, which was focused on a 5 μm spot at 40 mW. Before measurement, the micro-Raman system was calibrated using the 520 cm^{−1} peak of polycrystalline Si.

Transmission electron microscopy (TEM) was conducted at 220 kV with a Philips T30F field emission instrument equipped with a 2k-CCD camera and JEOL 2100F TEM equipped with a Schottky field-emission gun (FEG), with $C_s = 1.0$ mm operated at 200 kV. Double tilting was applied to find the right zone axis as required. The morphologies of the cathode and cathode/electrolyte interface were obtained using an environmental scanning electron microscope (ESEM, QUANTA-2000). The selected area electron diffraction (SAED) simulation patterns based on the XRD refinements results were obtained using the CrystalMaker (2.5.1) and SingleCrystal (2.0.1) software.²⁴

Electrochemical measurements

EIS of the cathode was obtained by AC impedance measurements using an electrochemical workstation composed of a Solartron 1260A frequency response analyser and a Solartron

1287 potentiostat. The symmetrical cells were tested between 450–750 °C in an ambient air atmosphere. The applied frequency range was from 0.01 Hz to 100 kHz, and the signal amplitude was 10 mV. The measurement was performed under an open cell voltage (OCV) condition. Electrode polarisation resistance data were analysed with Z-plot 3.0c software.

3. Results and discussion

Structure characterisation

Fig. 1a shows the XRD patterns of $\text{Sr}_{1-s}\text{Nb}_{0.1}\text{Co}_{0.9}\text{O}_{3-\delta}$ ($s = 0, 0.02$ and 0.05) powders calcined at 1200 °C. SNC1.00, SNC0.98 and SNC0.95 contain a single phase. A second phase, CoO, however appears on the XRD patterns when A-site deficiency was made in excess of 5% (ESI, Fig. S1†).

To avoid complications from the second phase, we limit our scope to SNC1.00, SNC0.98, and SNC0.95. SNC0.95 has a tetragonal structure, the symmetry of which can be described by the $P4/mmm$ space group (#123). This is implied by the line splitting of peaks at approximately 47°, 58.5° and 68.5°, which was not observed in SNC1.00 and SNC0.98 (Fig. 1b). Raman spectroscopy was used to probe the symmetry of the crystal structure of SNC1.00, SNC0.98, and SNC0.95 (Fig. 2). No vibrational modes were observed for SNC1.00, indicating high symmetry, *i.e.*, a $Pm\bar{3}m$ cubic symmetry.²⁵ Six modes were identified for SNC0.95, in agreement with the symmetry of the $P4/mmm$ space group.²⁶ We further confirmed the cubic and

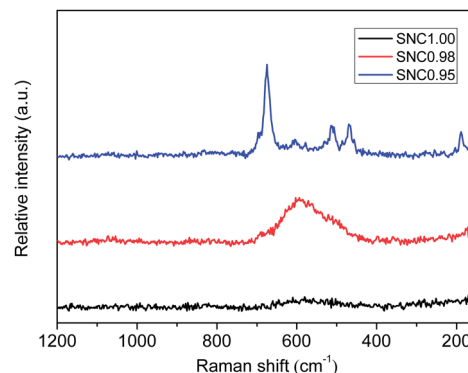


Fig. 2 Raman spectra of SNC1.00, SNC0.98 and SNC0.95.

tetragonal lattice for SNC1.00 and SNC0.95, respectively, by high resolution (HR) TEM and selected area electron diffraction (SAED) (Fig. 3). The HRTEM image and the corresponding SAED pattern of SNC1.00 are indeed characteristic of the primitive cubic perovskite symmetry best described by $Pm\bar{3}m$ space group (#221) with $a = a_p = 3.9$ Å. For SNC0.95, the reconstruction of the reciprocal space from the SAED pattern revealed a tetragonal cell with $a \approx a_p$ and $c \approx 2a_p$, compatible with the $P4/mmm$ space group. The doubled cell parameter value with respect to the primitive perovskite cell is clearly indicated on the HRTEM image and the corresponding SAED pattern.

The structure of SNC0.98 cannot be directly identified by XRD. SNC1.00 and SNC0.98 powders showed similar XRD patterns but distinct Raman vibrational modes (Fig. 2). The broad band at ~ 590 cm⁻¹ in the spectrum of SNC0.98 was indicative of degradation of ideal cubic symmetry; most likely attributed to a local JT distortion.²⁷ The JT distortion may lead to a tetragonal distortion in the CoO_6 octahedra.²⁷ Slight

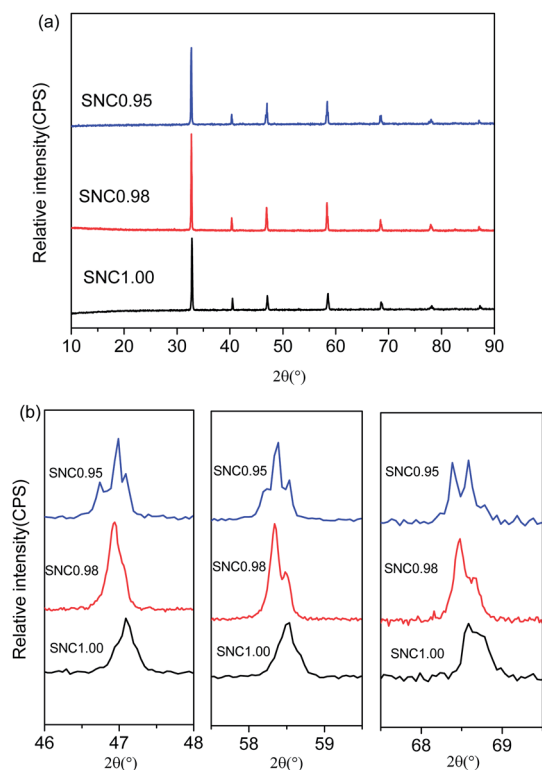


Fig. 1 (a) X-ray diffraction patterns of SNC1.00, SNC0.98 and SNC0.95 powders calcined at 1200 °C; (b) magnified XRD patterns around $2\theta = 47^\circ, 58.5^\circ$ and 68.5° .

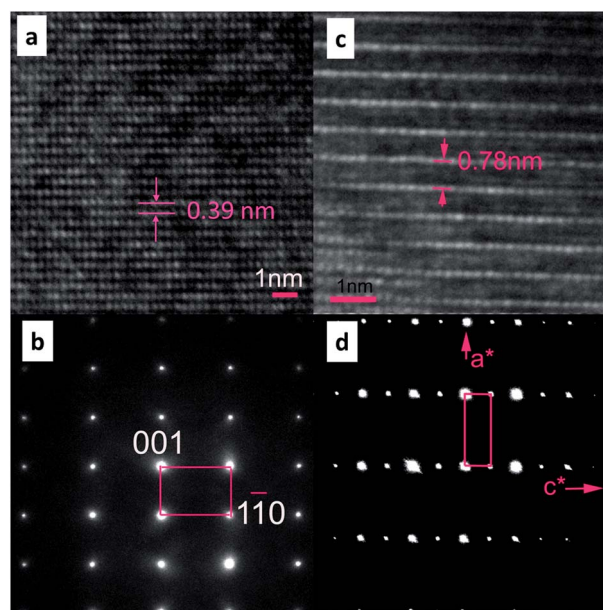


Fig. 3 HRTEM images of (a) SNC1.00 and (c) SNC0.95; SAED images of (b) SNC1.00 and (d) SNC0.95.²⁰

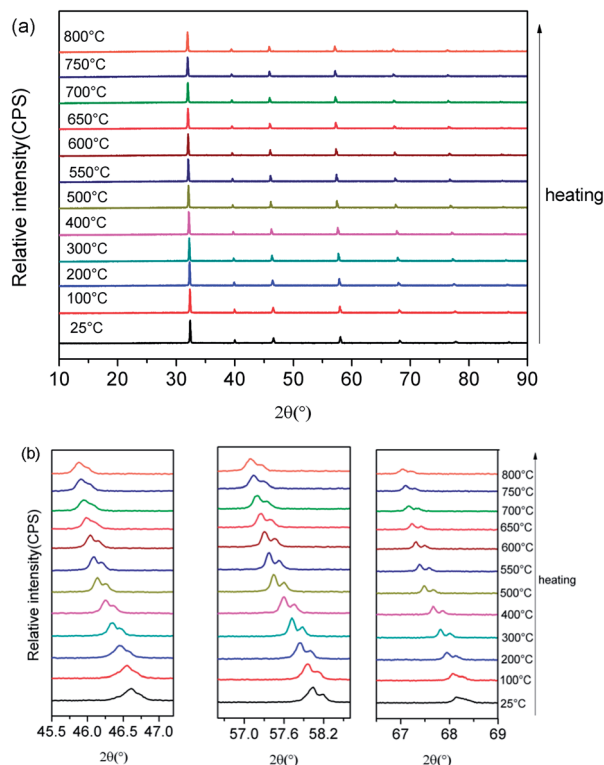


Fig. 4 (a) HT-XRD patterns of the SNC0.98 powder between room temperature to 800 °C. (b) Magnified XRD patterns around $2\theta = 47^\circ$, 58.5° and 68.5° .

decrease in the symmetry of the diffraction peaks (Fig. 1b) implies the likelihood of a $P4mm$ symmetry, as is the case of BaTiO_3 perovskite.²⁸ We refined the structure of SNC0.98 using model based on centrosymmetric $Pm\bar{3}m$, noncentrosymmetric $P4mm$ and centrosymmetric $P4/mmm$ space group. $P4mm$ space group (#99) model gave the lowest residuals among the three models (Table S1†). Low electrical conductivity SNC0.98 seems to somewhat correlate with the noncentrosymmetric structure as suggested by the following conductivity results. The phase stability was then probed using high-temperature (HT)-XRD (Fig. 4). The splitting of the peaks at 47° , 58.5° and 68° is retained up to 800 °C; ruling out the possible phase transformation during SOFC operation.

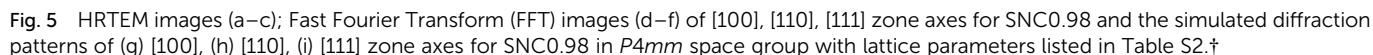
HRTEM was used to examine the crystal structure of SNC0.98. Fig. 5 indicates identical lattice structure between SNC0.98 and SNC1.00. It is not possible to confidently distinguish $P4mm$ from $Pm\bar{3}m$ symmetry using HRTEM and SAED results, considering the relatively weak tetragonal distortion as reflected by the ratio of c/a of only 1.003 (for $P4mm$ symmetry).²⁹ This is particularly apparent upon comparing the Fast Fourier Transform (FFT) images with the simulated electron diffraction spots (Fig. 5d–f to g–i).

Lattice parameters of SNC1.00, SNC0.98 and SNC0.95 were obtained by Rietveld refinement (Fig. S2 and Table S2†). Introduction of A-site defects in $\text{Sr}_{1-s}\text{Nb}_{0.1}\text{Co}_{0.9}\text{O}_{3-\delta}$ perovskites led to lattice expansion for both SNC0.98 and SNC0.95. The (Co,Nb)–O bond lengths and O–(Co,Nb)–O angles in SNC1.00, SNC0.98 and SNC0.95 are listed in Table 1. The crystal structure

transitions from $Pm\bar{3}m$ to $P4mm$ and $P4/mmm$ are depicted schematically in Fig. 6. The $P4mm$ structure exemplified a tetragonal distortion of the cubic perovskite, resulting in a difference of (Co,Nb)– O_1 and (Co,Nb)– O_1^* bond lengths. As a result, (Co,Nb)– O_1^* bond can be visualised to be excluded from an originally symmetric (Co,Nb) O_6 octahedron (imagine taking out O_1^* from one of the opposing apex) so that the repeating unit becomes a distorted (Co,Nb) O_5 square pyramid which shares corner with other units (in the same layer). For 0.05 A-site deficiency case, although each (Co,Nb)– O_1^* and (Co,Nb)– O_1 bond shows similar bond length value (1.8810 Å and 2.0075 Å, respectively), they are distributed periodically in two different (Co,Nb) O_6 octahedron, forming an overall framework described by $P4/mmm$ symmetry. Perhaps, the doubling of the lattice in SNC0.95 originates from long-range ordering of oxygen vacancies along the c axis, which brings about the charge-ordering between Co^{4+} and Co^{3+} cations. Charge ordering is a phase transition observed mostly in strongly correlated materials such as transition metal oxides.^{30–32} Strong interaction between electrons in these materials lead to localised charges on different sites and thus, a disproportionation and an ordered superlattice.³³ Here, two types of (Co,Nb) O_6 octahedron exist within the $P4/mmm$ framework; the elongated one *e.g.* (Co,Nb) 1O_6 octahedron containing two stacked (Co,Nb) 1–O_2 bonds of 2.0075 Å length each (as the 4-fold axis) while the shortened one *e.g.* (Co,Nb) 2O_6 octahedron containing two stacked (Co,Nb) 2–O_2 bonds of 1.8810 Å length each (also as 4-fold axis). In both cases, the square centre of the octahedron is symmetrical as reflected by 4 equivalent bond length of (Co,Nb) 1–O_1 and (Co,Nb) 2–O_3 (*e.g.* 1.9348 Å). Since the average valence for Co is 3.2^+ (Table 2), the charge-ordering hypothesis signifies an average oxidation state of Co^{3+} at (Co,Nb) 1O_6 sites and $\text{Co}^{3.4+}$ at (Co,Nb) 2O_6 sites, assuming a full charge disproportionation. A similar structure was also noticed earlier in a $\text{SrSb}_{0.1}\text{Co}_{0.9}\text{O}_{3-\delta}$ perovskite.³⁴

We speculate that the JT distortion offsets the increased energy of the perovskite system induced by a 2% A-site deficiency. Nonetheless, increasing the deficiency to 5% cannot be compensated by slight (local) JT distortion. SNC0.95 shows substantial JT distortion reflected by (Co,Nb) 1O_6 with elongated axial bond and (Co,Nb) 2O_6 with shortened axial bond. Both distortions will lower the energy for a system with one e_g electron (for (Co,Nb) 1O_6 the z^2 orbital is lowered and x^2-y^2 orbital for (Co,Nb) 2O_6 just the opposite direction, and in both cases the lowest e_g orbital is singly occupied). Therefore, besides the JT distortion, the elastic energy would be further minimised by such an ordering with shorter and longer bond lengths.^{22,35,36}

Within the perovskite, each O^{2-} is surrounded by 4 A-site cations and 2 B-site cations. The formation of one A-site vacancy necessitates a change in the local coordination number (CN) from 6 to 5 for O^{2-} . Given that no O^{2-} ions with CN = 5 is possible,³⁷ the distortions of the oxygen sublattice somehow need to be compensated by modifying the perovskite structure. $\text{La}_{1/3}\text{NbO}_3$, for example can accommodate a large A-site deficiency since Nb–O has a high degree of covalence to stabilise the Nb–O network.³⁸ However, for transition metal cations which can easily change their oxidation states (such as Co), a stable

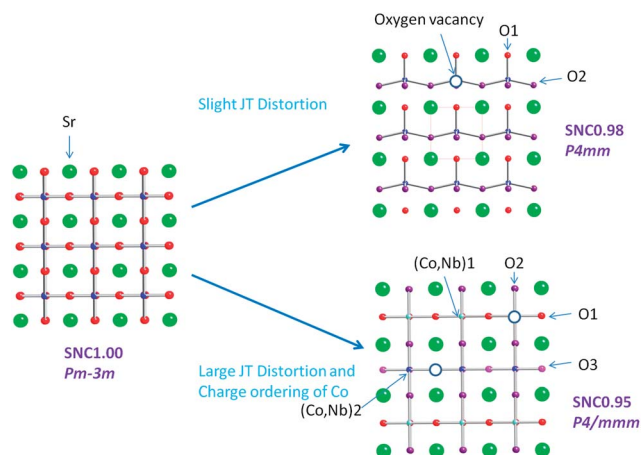


SNC0.95 (-287 kJ mol^{-1} , ESI, Fig. S4†). The obtaining of 5% A-site deficient (SNC0.95) perovskite phase here highlights the fact that the stability of B-site octahedron provides a more dominant role.

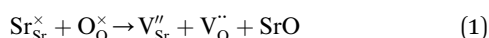
In general, additional oxygen vacancies may negatively impact the electronic transport; normally evidenced by a decrease in the electrical conductivities (of some A-site deficient perovskites).^{10,14,19,39} Fig. 7 depicts the oxygen vacancy concentrations of SNC1.00, SNC0.98, and SNC0.95 between 450–800 °C.

Table 1 (Co,Nb)–O bond lengths and angles of O–(Co,Nb)–O for SNC1.00, SNC0.98 (*P4mm* symmetry) and SNC0.95

SNC1.00			
(Co,Nb)–O × 6	1.936(3)	O–(Co,Nb)–O	180°
SNC0.98			
(Co,Nb)–O ₁	1.837(0)	O ₁ –(Co,Nb)–O ₁ *	180°
(Co,Nb)–O ₁ *	2.055(2)		
(Co,Nb)O ₂ × 4	1.986(9)	O ₂ –(Co,Nb)–O ₂	154.92°
SNC0.95			
(Co,Nb)1–O ₂ × 2	2.007(5)	O ₂ –(Co,Nb)1–O ₂	180°
(Co,Nb)2–O ₂ × 2	1.881(0)	O ₂ –(Co,Nb)2–O ₂	180°
(Co,Nb)1–O ₁ × 4	1.934(8)	O ₁ –(Co,Nb)1–O ₁	180°
(Co,Nb)2–O ₃ × 4	1.934(8)	O ₃ –(Co,Nb)2–O ₃	180°

**Fig. 6** Schematic of the structure transition from *Pm* $\bar{3}$ *m* (SNC1.00) to *P4mm* (SNC0.98) and *P4/mmm* (SNC0.95).

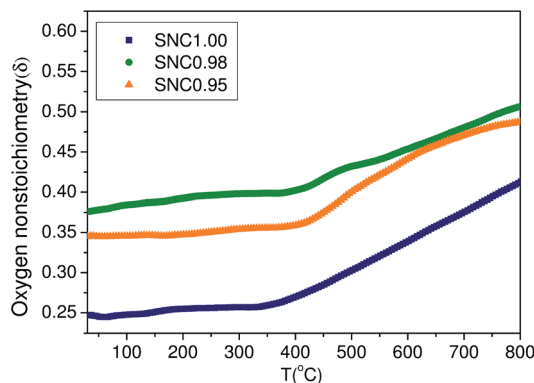
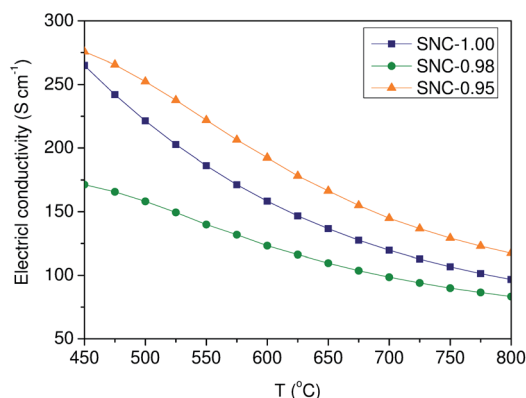
Additional oxygen vacancies actually formed with the increase in A-site defects as described by eqn (1).



SNC0.98 has the largest oxygen vacancy concentration in the temperature range studied. Fig. 8 displays the electrical conductivities of SNC1.00, SNC0.98 and SNC0.95 between 450–800 °C. Whilst reduced electrical conductivity of SNC0.98 (relative to SNC1.00) is consistent with its higher concentration of oxygen vacancies, SNC0.95 deviates from this trend. Despite its larger concentration of oxygen vacancies, in fact, the electrical conductivity of SNC0.95 exhibits values between 276–117 S cm^{−1},²⁰ higher than those of 265–83 S cm^{−1} for SNC1.00. This

Table 2 Valence states of cobalt and oxygen non-stoichiometry (δ) of SNC1.00, SNC0.98 and SNC0.95 at room temperature

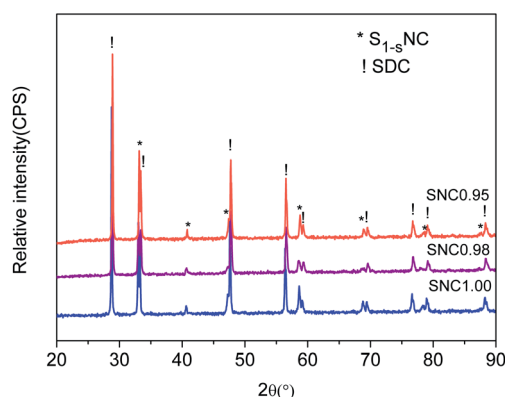
Sample	δ	Valence states of cobalt
SNC1.00	0.24	3.3
SNC0.98	0.38	3.0
SNC0.95	0.35	3.2

**Fig. 7** Oxygen vacancy concentrations of SNC1.00, SNC0.98 and SNC0.95 between 25–800 °C.**Fig. 8** Electrical conductivities of SNC1.00, SNC0.98 and SNC0.95 (ref. 20) between 450–800 °C.

synergistic effect is perhaps related to its intrinsic structure with *P4/mmm* symmetry. It is very likely that the charge ordering of Co favours rapid electron transport in SNC0.95.

Chemical and thermal compatibility

Several A-site deficient perovskites, such as (La,Sr)MnO₃ (LSM) and (La,Sr)FeO₃ (LSF) displayed good chemical compatibility with YSZ electrolytes; associated with the absence of highly

**Fig. 9** XRD patterns of SNC1.00-SDC, SNC0.98-SDC and SNC0.95-SDC²⁰ mixed powders (1 : 1 weight ratio) calcined at 1000 °C for 2 h.

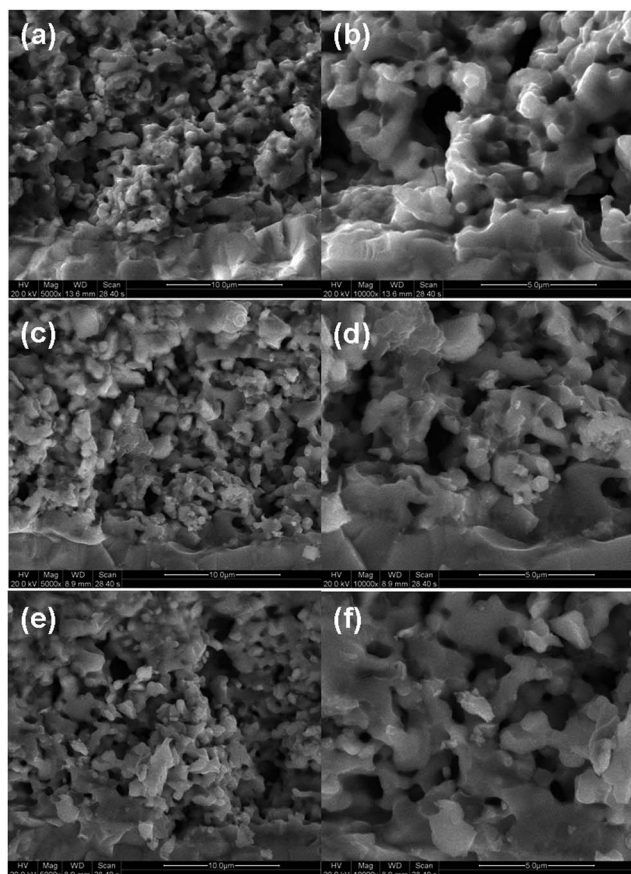


Fig. 10 SEM images of (a and b) SNC1.00, (c and d) SNC0.98 and (e and f) SNC0.95 cathodes calcined at 1000 °C for 2 h in air. The scale bars are 10 μm for (a), (c) and (e) and 5 μm for (b), (d) and (f).

resistive SrZrO_3 and $\text{La}_2\text{Zr}_2\text{O}_7$ phases at the electrode–electrolyte interface.^{40,41} However, in a previous study, we reported that introducing A-site deficiency led to detrimental phase reactions between (A-site-deficient) $\text{Ba}_{0.5}\text{Sr}_{0.5}\text{Co}_{0.8}\text{Fe}_{0.2}\text{O}_{3-\delta}$ (BSCF) perovskites and $\text{Sm}_{0.2}\text{Ce}_{0.8}\text{O}_{1.9}$ (SDC) at 1000 °C during which inert phase(s) formed which inhibited the ORR.¹⁴ Fig. 9 shows the XRD patterns of $\text{Sr}_{1-s}\text{Nb}_{0.1}\text{Co}_{0.9}\text{O}_{3-\delta}$ –SDC mixed powders (1 : 1 weight ratio) calcined at 1000 °C. No other diffraction peaks apart from those characteristics of single-phase $\text{Sr}_{1-s}\text{Nb}_{0.1}\text{Co}_{0.9}\text{O}_{3-\delta}$ and SDC were perceived. This indicates good chemical compatibility of $\text{Sr}_{1-s}\text{Nb}_{0.1}\text{Co}_{0.9}\text{O}_{3-\delta}$ perovskites against SDC electrolytes.

The microstructures of the $\text{Sr}_{1-s}\text{Nb}_{0.1}\text{Co}_{0.9}\text{O}_{3-\delta}$ cathodes are shown in Fig. 10. Firm attachment between the cathode and electrolyte suggests good thermal compatibility between $\text{Sr}_{1-s}\text{Nb}_{0.1}\text{Co}_{0.9}\text{O}_{3-\delta}$ perovskites and SDC. The grain sizes and pore structures look very similar for the three cathodes, which dismisses microstructural effects on the electrochemical performance.

Oxygen reduction reaction activity

Fig. 11 shows typical impedance spectra for the $\text{Sr}_{1-s}\text{Nb}_{0.1}\text{Co}_{0.9}\text{O}_{3-\delta}$ cathodes between 550–650 °C. The difference between the intercepts of the impedance arc on the real axis is the interfacial

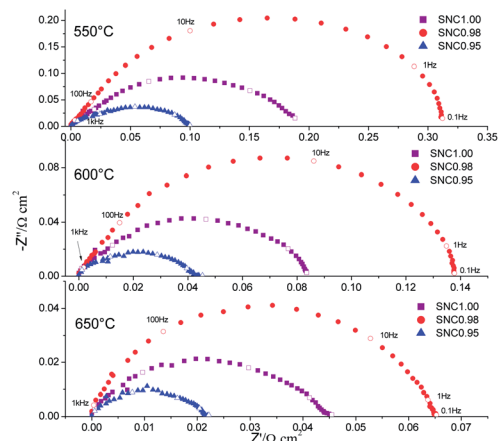


Fig. 11 Electrochemical impedance spectra of SNC1.00, SNC0.98 and SNC0.95 cathodes between 550–650 °C.

resistance of the cathode, denoted as the area specific resistance (ASR). The ASRs were measured to be 0.19, 0.31 and 0.10 $\Omega \text{ cm}^2$ for SNC1.00, SNC0.98, and SNC0.95 at 550 °C, respectively. Fig. 12 shows the thermal evolution of the ASR values of the three cathodes prepared under identical conditions. Since ASRs measured on porous electrodes are susceptible to changes in morphology of the electrodes, each data point was taken from three measurements on three different specimens (with same composition). The microstructure and thickness of all electrodes are very similar to each other (Fig. S5†). The SNC0.95 cathode showed lower ASR values relative to SNC1.00, whereas the SNC0.98 cathode displays lower ORR activity with respect to SNC1.00. With negligible effects from microstructure and reaction between cathode and electrolyte, the observed trend closely represents the intrinsic properties of $\text{Sr}_{1-s}\text{Nb}_{0.1}\text{Co}_{0.9}\text{O}_{3-\delta}$. Within the context of correlating structure–electrochemical properties specific to $\text{Sr}_{1-s}\text{Nb}_{0.1}\text{Co}_{0.9}\text{O}_{3-\delta}$, a (slight) local JT distortion seems to contribute negatively towards the electron transport and the ORR activity.

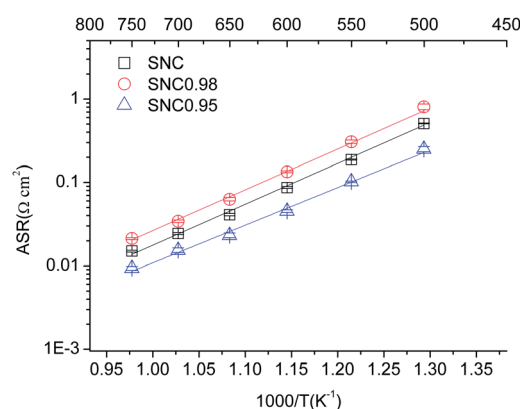


Fig. 12 Temperature dependent ASRs of $\text{Sr}_{1-s}\text{Nb}_{0.1}\text{Co}_{0.9}\text{O}_{3-\delta}$ cathodes tested between 500 and 750 °C. Error bars represent standard deviations of three independent measurements.

4. Conclusions

In summary, we demonstrated the effect of crystal structure on the ORR activity of SNC0.98 and SNC0.95 cathodes. Relative to SNC1.00 ($Pm\bar{3}m$ symmetry), SNC0.95 ($P4/mmm$ symmetry) which displays a large JT distortion in combination with charge-ordering of Co, shows improved ORR activity at low temperature, whereas SNC0.98 ($P4mm$ symmetry) which exhibits slight (local) JT distortion, shows lower performance.

Acknowledgements

This work was supported by the China National Funds to Distinguished Young Scientists under no. 51025209, the Outstanding Young Scholar Grant at Jiangsu Province under no. 2008023, the Fok Ying Tung Education Grant under contract no. 111073, the Program for New Century Excellent Talents in Chinese Ministry of Education and the National Basic Research Program of China under contract no. 2007CB209704, and Australian Research Council (ARC). YL and FC were supported by the HeteroFoam Center, an Energy Frontier Research Center funded by Office of Science, U.S. Department of Energy under Award Number DE-SC0001061. Electron microscopy research was partially carried out at the Center for Functional Nanomaterials, Brookhaven National Laboratory, which is supported by the U.S. Department of Energy, Office of Basic Energy Sciences, under contract no. DE-AC02-98CH10886. XS thanks the China Scholarship Council and Brookhaven National Laboratory for the financial support for his exchange program.

Notes and references

- 1 H. U. Anderson, *Solid State Ionics*, 1992, **52**, 33.
- 2 B. C. H. Steel and A. Heinzel, *Nature*, 2001, **414**, 345.
- 3 Z. P. Shao and S. M. Haile, *Nature*, 2004, **431**, 170.
- 4 Z. P. Shao, W. S. Yang, Y. Cong, H. Dong, J. H. Dong and G. Q. Xiong, *J. Membr. Sci.*, 2000, **172**, 177.
- 5 Q. M. Li, X. F. Zhu, Y. F. He and W. S. Yang, *Catal. Today*, 2000, **149**, 185.
- 6 J. H. Kim, M. Cassidy, J. T. S. Irvine and J. Bae, *Chem. Mater.*, 2010, **22**, 883.
- 7 T. Hibino, A. Hashimoto, T. Inoue, J. Tokuno, S. Yoshida and M. Sano, *Science*, 2000, **288**, 2031.
- 8 T. Z. Sholklapper, H. Kurokawa, C. P. Jacobson, S. J. Visco and L. C. De Jonghe, *Nano Lett.*, 2007, **7**, 2136.
- 9 J. B. Goodenough, *Rep. Prog. Phys.*, 2004, **67**, 1915.
- 10 G. C. Kostogloudis and C. Ftikos, *Solid State Ionics*, 1999, **126**, 143.
- 11 K. K. Hansen, *J. Electrochem. Soc.*, 2009, **156**, B1257.
- 12 E. Konyshcheva and J. T. S. Irvine, *J. Mater. Chem.*, 2008, **18**, 5147.
- 13 J. Knudsen, P. B. Friehling and N. Bonanos, *Solid State Ionics*, 2005, **176**, 1563.
- 14 W. Zhou, R. Ran, Z. P. Shao, W. Q. Jin and N. P. Xu, *J. Power Sources*, 2008, **182**, 24.
- 15 Z. B. Yang, C. H. Yang, C. Jin, M. F. Han and F. L. Chen, *Electrochem. Commun.*, 2011, **13**, 882.
- 16 Z. Liu, L. Z. Cheng and M. F. Han, *J. Power Sources*, 2011, **196**, 868.
- 17 Z. B. Yang, M. F. Han, P. Y. Zhu, F. Zhao and F. L. Chen, *Int. J. Hydrogen Energy*, 2011, **36**, 9162.
- 18 K. K. Hansen and K. V. Hansen, *Solid State Ionics*, 2007, **178**, 1379.
- 19 A. Mineshige, J. Izutsu, M. Nakamura, K. Nigaki, J. Abe, M. Kobune, S. Fujii and T. Yazawa, *Solid State Ionics*, 2005, **176**, 1145.
- 20 Y. L. Zhu, Z. G. Chen, W. Zhou, S. S. Jiang, J. Zou and Z. P. Shao, *ChemSusChem*, 2013, **6**, 2294.
- 21 W. Zhou, Z. P. Shao, R. Ran, W. Q. Jin and N. P. Xu, *Chem. Commun.*, 2008, 5791.
- 22 W. Zhou, J. Sunraso, Z. G. Chen, L. Ge, J. Motuzas, J. Zou, G. X. Wang, A. Julbe and Z. H. Zhu, *Energy Environ. Sci.*, 2011, **4**, 872.
- 23 *DIFFRACPlus TOPAS 4.2 software*, Bruker-AXS GmbH, Karlsruhe, Germany, 2008.
- 24 *CrystalMaker and SingleCrystal software*, CrystalMaker Software Ltd., Oxford, England, 2014.
- 25 E. Granado, N. O. Moreno, A. García, J. A. Sanjurjo, C. Rettori, I. Torriani, S. B. Oseroff, J. J. Neumeier, K. J. McClellan, S. W. Cheong and T. Tokura, *Phys. Rev. B: Condens. Matter Mater. Phys.*, 1998, **58**, 11435.
- 26 R. Lownders, M. Deluca, F. Azough and R. Freer, *J. Appl. Phys.*, 2013, **113**, 044115.
- 27 S. Gangopadhyay, T. Inerbaev, A. E. Masunov, D. Altilio and N. Orlovskaya, *ACS Appl. Mater. Interfaces*, 2009, **7**, 1512.
- 28 B. D. Begg, K. S. Finnie and E. R. Vance, *J. Am. Ceram. Soc.*, 1996, **79**, 2666.
- 29 M. Otonicar, S. D. Skapin, B. Jancar, R. Uvic and D. Suvorov, *J. Am. Ceram. Soc.*, 2010, **93**, 4168.
- 30 Y. Tokura and N. Nagaosa, *Science*, 2000, **288**, 462.
- 31 G. Kotliar and D. Vollhardt, *Phys. Today*, 2004, **57**, 53.
- 32 E. Dagotto, *Science*, 2005, **309**, 257.
- 33 T. Goto and B. Lüthi, *Adv. Phys.*, 2003, **52**, 67.
- 34 A. Aguadero, C. de la Calle, J. A. Alonso, M. J. Escudero, M. T. Fernández-Díaz and L. Daza, *Chem. Mater.*, 2007, **19**, 6437.
- 35 W. Zhou, J. Sunarso, J. Motuzas, F. L. Liang, Z. G. Chen, L. Ge, S. M. Liu, A. Julbe and Z. H. Zhu, *Chem. Mater.*, 2011, **23**, 1618.
- 36 Y. Li, J. G. Cheng, J. Song, J. A. Alonso, M. T. Fernández-Díaz and J. B. Goodenough, *Chem. Mater.*, 2012, **24**, 4114.
- 37 R. D. Shannon and C. T. Rettitt, *Acta Crystallogr., Sect. B: Struct. Crystallogr. Cryst. Chem.*, 1969, **25**, 925.
- 38 E. Konyshcheva, X. X. Xu and J. T. S. Irvine, *Adv. Mater.*, 2012, **24**, 528.
- 39 X. Li, H. L. Zhao, X. O. Zhou, N. S. Xu, Z. X. Xie and N. Chen, *Int. J. Hydrogen Energy*, 2010, **35**, 7931.
- 40 D. L. Meixner and R. A. Cutler, *Solid State Ionics*, 2002, **146**, 273.
- 41 U. F. Vogt, P. Holtappels, J. Sfeir, J. Richter, S. Duval, D. Wiedenmann and A. Züttel, *Fuel Cells*, 2009, **9**, 899.